

HalluGen: Synthesizing Realistic and Controllable Hallucinations for Evaluating Image Restoration

Seunghoi Kim^{1,2*} Henry F. J. Tregidgo^{1,2} Chen Jin⁴ Matteo Figini^{1,3} Daniel C. Alexander^{1,3}
¹ Hawkes Institute, UCL ² Dept. of Medical Physics and Biomedical Engineering, UCL
³ Dept. of Computer Science, UCL ⁴ Centre for AI, DS&AI, AstraZeneca, UK

Abstract

Generative models are prone to hallucinations: plausible but incorrect structures absent in the ground truth. This issue is problematic in image restoration for safety-critical domains such as medical imaging, industrial inspection, and remote sensing, where such errors undermine reliability and trust. For example, in low-field MRI, widely used in resource-limited settings, restoration models are essential for enhancing low-quality scans, yet hallucinations can lead to serious diagnostic errors. Progress has been hindered by a circular dependency: evaluating hallucinations requires labeled data, yet such labels are costly and subjective. We introduce HalluGen, a diffusion-based framework that synthesizes realistic hallucinations with controllable type, location, and severity, producing perceptually realistic but semantically incorrect outputs (segmentation IoU drops from 0.86 to 0.36). Using HalluGen, we construct the first large-scale hallucination dataset comprising 4,350 annotated images derived from 1,450 brain MR images for low-field enhancement, enabling systematic evaluation of hallucination detection and mitigation. We demonstrate its utility in two applications: (1) benchmarking image quality metrics and developing Semantic Hallucination Assessment via Feature Evaluation (SHAFE), a feature-based metric with soft-attention pooling that improves hallucination sensitivity over traditional metrics; and (2) training reference-free hallucination detectors that generalize to real restoration failures. Together, HalluGen and its open dataset establish the first scalable foundation for evaluating hallucinations in safety-critical image restoration. We will make the code and dataset publicly available upon acceptance.

1. Introduction

Hallucinations, visually plausible yet incorrect content, are a fundamental failure mode of modern generative models. In image restoration, where models reconstruct missing in-

formation from degraded measurements, such errors can be especially harmful in safety-critical domains such as medical imaging, industrial inspection, and remote sensing. Unlike adversarial attacks, hallucinations arise naturally from generative uncertainty.

Despite recent advances in image restoration [8, 25, 30, 31, 36, 44], these models still produce hallucinations that are difficult to detect or measure. As shown in Fig. 1 (top), progress is limited by a *circular dependency*: hallucination analysis requires labeled data, yet hallucinations are ambiguous and costly to annotate. Measuring hallucinations is non-trivial as common metrics (PSNR, SSIM, LPIPS [52]) favor perceptual sharpness over correctness, often scoring hallucinated outputs highly. Existing evaluations rely on downstream task performance [21–23] or manual labels [2, 34], which either conflate hallucinations with task accuracy or are restricted to simple datasets (e.g., MNIST [27], Hands [1]).

To break this deadlock, we introduce *HalluGen*, a diffusion-based framework for controllable and realistic hallucination generation. Following recent work [6, 23], we categorize hallucinations as (1) *intrinsic*, which break measurement consistency, and (2) *extrinsic*, which remain consistent but are semantically incorrect.

HalluGen extends diffusion-based inverse solvers with targeted gradient perturbations, enabling explicit control over hallucination *type, location, and severity*. Controllability is crucial as hallucinations in decision-critical regions (e.g., lesions, solder joints) pose the greatest risk. To the best of our knowledge, no prior work enables controllable, taxonomically grounded hallucination synthesis for systematic hallucination analysis in image restoration. We instantiate HalluGen with Diffusion Posterior Sampling [10], though it is compatible with other diffusion formulations.

Our contributions are threefold:

1. We propose *HalluGen*, a diffusion-based framework for controllable hallucination generation in image restoration, generalizing across medical (HCP) [41], industrial (MVTec AD [5]), and natural (ImageNet [12]) images.
2. Using HalluGen, we construct the *first large-scale hal-*

*Correspondence to: seunghoi.kim.17@ucl.ac.uk

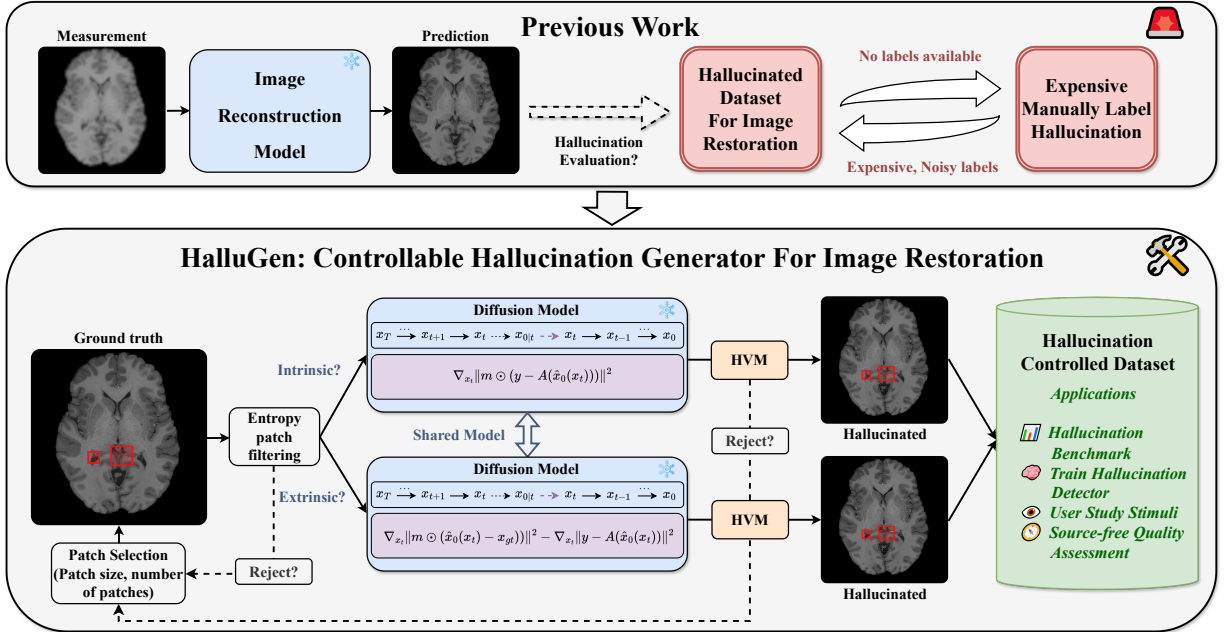


Figure 1. **Circular dependency in hallucination evaluation and our proposed HalluGen solution.** Top: Reliable hallucination analysis requires labeled data, but obtaining labels demands expert annotation with high disagreement. Bottom: HalluGen breaks this loop by generating controllable hallucinations with automatic labels, enabling systematic benchmarking, and perceptual studies across domains.

lucination dataset for low-field MRI enhancement, comprising 4,350 predictions with patch-level annotations across 1,450 images. This dataset establishes a foundation for systematic hallucination analysis.

- Using the HalluGen-generated dataset, we demonstrate two key applications: (a) a *hallucination metric benchmark*, revealing that existing metrics overlook hallucinations. We develop *Semantic Hallucination Assessment via Feature Evaluation (SHAFE)*, a feature-based metric with soft-attention pooling that improves hallucination detection AUC by 0.25 and reduces false negatives by 24 percentage points; and (b) *reference-free hallucination detectors* trained on HalluGen and evaluated on real restoration outputs without ground-truth references.

Together, HalluGen and our dataset establish the first systematic foundation for generating and evaluating hallucinations in image restoration, advancing toward safer and more reliable deployment in safety-critical applications.

2. Related Work

2.1. Image Restoration

Image restoration aims to recover clean, high-quality images from degraded measurements across tasks such as super-resolution, denoising, and deblurring. Modern supervised models learn powerful data-driven priors for perceptual quality [8, 14, 30, 31, 44], while recent works leverage pre-trained diffusion models as generative priors

for inverse problems [10, 11, 20, 38, 45, 50, 54]. These approaches have been extended to medical imaging, including compressed sensing and low-field MRI enhancement [3, 15, 18, 23, 26, 32, 42]. However, emphasizing perceptual realism can induce hallucinations, plausible but incorrect structures, reflecting the perception–distortion trade-off [7, 44]. In safety-critical domains, hallucination is a known risk but remains largely unstudied, with only a few recent work [2, 22, 23, 34] proposing mitigation strategies.

2.2. Image Quality Metrics

Traditional full-reference metrics [39, 47, 53] focus on pixel-wise fidelity and global structural similarity, making them sensitive to misalignment and ineffective at capturing localized or semantically incorrect errors. Learned perceptual metrics [13, 52] improve correlation with human perception by comparing deep feature representations, but they aggregate errors globally and remain insensitive to spatially sparse hallucinations. In medical image reconstruction, recent efforts to quantify hallucinations [6, 43] are restricted to linear forward models or task-specific architectures, limiting generality. These limitations motivate the SHAFE metric (Section 4.5), which computes local (e.g. patch) metric maps and aggregates them using soft-attention weighting, increasing sensitivity to localized hallucinations.

2.3. Hallucination Benchmarks

Recent benchmarks for language and vision-language models (LLMs and VLMs) evaluate semantic hallucinations such as factually incorrect or unverifiable outputs. Examples include HaluEval, HalluLens, and HallusionBench for text–image reasoning [4, 16, 28], POPE for object hallucination [29], and VideoHalluciner for temporal hallucination analysis [46]. While some recent works [19, 35, 48] attempt to synthesize hallucinations to automate annotation in VLMs, they lack spatial control (e.g., size, location) over how hallucinations are generated. To our knowledge, no benchmark exists for hallucinations in image restoration with spatial annotations, a gap our work addresses.

3. Method

3.1. Problem Formulation

Image restoration aims to recover a high-quality image $x \in \mathbb{R}^N$ from its degraded observation $y \in \mathbb{R}^M$, formulated as an inverse problem:

$$y = \mathcal{A}(x) + n, \quad (1)$$

where $\mathcal{A}(\cdot)$ denotes the forward degradation operator and n is measurement noise. As \mathcal{A} is typically non-invertible, recovery is ill-posed.

Hallucination Taxonomy. We categorize hallucinations based on their relationship to the forward operator $\mathcal{A}(\cdot)$, following the recent work on hallucination [6, 23].

Intrinsic hallucinations violate measurement consistency, introducing features inconsistent with observed data:

$$\mathcal{A}(\hat{x}) \neq \mathcal{A}(x_{\text{gt}}), \quad (2)$$

where \hat{x} and x_{gt} denote the reconstructed image and ground truth, respectively.

Extrinsic hallucinations preserve measurement consistency but differ in the inverse domain of \mathcal{A} :

$$\mathcal{A}(\hat{x}) = \mathcal{A}(x_{\text{gt}}), \text{ but } \mathcal{A}^{-1}(\mathcal{A}(\hat{x})) \neq \mathcal{A}^{-1}(\mathcal{A}(x_{\text{gt}})). \quad (3)$$

This distinction is crucial: intrinsic hallucinations can be detected through measurement consistency checks, while extrinsic hallucinations require ground truth or domain knowledge. In medical imaging, both pose serious risks as they may obscure clinically significant details. Understanding and systematically evaluating both categories motivates the need for controlled hallucination generation.

3.2. Why do we need hallucination generator?

Existing metrics are insensitive to hallucinations. Figure 2 shows that standard image quality metrics (PSNR, SSIM, LPIPS) assign higher scores to hallucinated predictions from pretrained conditional diffusion models on

MVTec AD [5] and BraTS [33] than to slightly blurred but semantically correct images. This exposes a critical flaw: these metrics favor perceptual sharpness over correctness of content, failing to penalize plausible yet false features. Such bias highlights the need for hallucination-aware evaluation, which requires labeled hallucination data, a challenging circular dependency between generation and evaluation.

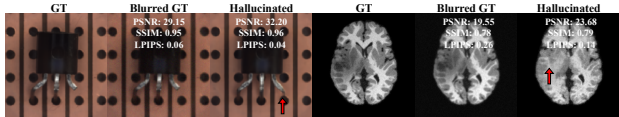


Figure 2. **Existing metrics fail to penalize hallucinations.** Across MVTEC AD (left) and BraTS (right), PSNR, SSIM, and LPIPS assign higher scores to hallucinated predictions than to slightly blurred but correct images, reflecting a bias toward perceptual sharpness over correctness.

Manual labeling is unreliable and uncontrolled. An intuitive approach to hallucination evaluation is manual annotation, but it is neither scalable nor reliable. To verify this, two domain experts annotated hallucination regions at the *patch level* across 50 images, yet the inter-annotator agreement was low (Cohen’s $\kappa = 0.30$), far below the accepted threshold ($\kappa > 0.60$). This highlights the subjective and ambiguous nature of spatial hallucination identification. These limitations motivate *HalluGen*, which synthesizes realistic hallucinations with known ground truth, enabling reproducible and scalable benchmarking.

3.3. HalluGen

Background: Diffusion Posterior Sampling. We build on denoising diffusion probabilistic models (DDPMs) [17] as our generative prior. Given a clean image x_0 , the forward process gradually adds Gaussian noise:

$$q(x_t|x_0) = \mathcal{N}(x_t; \sqrt{\bar{\alpha}_t}x_0, (1 - \bar{\alpha}_t)I), \quad (4)$$

where x_t denotes the noisy image at timestep t , $\bar{\alpha}_t = \prod_{i=1}^t(1 - \beta_i)$, β_t is the noise schedule. The reverse process denoises from $t = T$ to 0 using a learned model, where T is the total number of diffusion timesteps.

To solve inverse problems, Diffusion Posterior Sampling (DPS) [10] injects data consistency into the reverse process. At each step, a gradient update enforces the measurement constraint $y = \mathcal{A}(x)$:

$$x_{t-1} = \mu_\theta(x_t, t) - \lambda_t \nabla_{x_t} \|y - \mathcal{A}(\hat{x}_0(x_t))\|^2 + \sigma_t \epsilon, \quad (5)$$

where μ_θ is the model-predicted mean, $\hat{x}_0(x_t)$ is the Tweedie estimate of the clean image, λ_t controls guidance strength, and $\epsilon \sim \mathcal{N}(0, I)$. This steers sampling toward solutions consistent with the measurement y .

Intrinsic Hallucination Generation. HalluGen enables spatially controllable hallucination synthesis by operating

at the patch level. It samples random binary masks $m \in \{0, 1\}^{H \times W}$ that define injection regions, varying patch sizes to create hallucinations at different spatial scales. To induce intrinsic hallucinations that violate measurement consistency, HalluGen applies gradient *ascent* on the data-consistency term within masked regions (pushing away from consistency) and gradient *descent* outside. This process can be formulated as:

$$x_{t-1} = \mu_\theta(x_t, t) - \lambda_t \nabla_{x_t} \|(1 - m) \odot (y - \mathcal{A}(\hat{x}_0(x_t)))\|^2 + \gamma_t \cdot \nabla_{x_t} \|m \odot (y - \mathcal{A}(\hat{x}_0(x_t)))\|^2, \quad (6)$$

where $\gamma > 0$ controls the ascent strength. This formulation creates measurement space violations $\mathcal{A}(\hat{x}) \neq \mathcal{A}(x_{\text{gt}})$ specifically within the masked patches, generating intrinsic hallucinations while preserving fidelity elsewhere.

Extrinsic Hallucination Generation. Extrinsic hallucinations occur when reconstructions deviate in regions imperceptible to the forward operator while preserving measurement consistency. For general (nonlinear) operators $\mathcal{A}(\cdot)$, such regions, analogous to a null space, cannot be computed explicitly. HalluGen therefore applies gradient *ascent* in the ground-truth image space to induce semantic deviations while maintaining measurement fidelity.

However, pixel-space divergence alone yields suboptimal results, as the optimization seeks a compromise between three constraints: the learned data distribution $p_{\text{data}}(x)$, measurement consistency, and ground-truth divergence. To address this issue, we incorporate feature-space divergence using a pretrained feature extractor $F(\cdot)$ (e.g., DINO [40], SAM [24], MedSAM [9]):

$$x_{t-1} = \mu_\theta(x_t, t) - \lambda_t \odot \nabla_{x_t} \|y - \mathcal{A}(\hat{x}_0(x_t))\|^2 + \gamma_{1,t} \cdot \nabla_{x_t} \|m \odot (\hat{x}_0(x_t) - x_{\text{gt}})\|^2 + \gamma_{2,t} \cdot \nabla_{x_t} \|m \odot (F(\hat{x}_0(x_t)) - F(x_{\text{gt}}))\|^2, \quad (7)$$

where $\gamma_{1,t}$ and $\gamma_{2,t}$ control pixel- and feature-space divergence strengths at time step t . This generates semantically meaningful hallucinations that maintain visual realism while deviating substantially in feature space.

Hallucination Verification Module (HVM). To ensure hallucinations remain visually plausible yet perceptually distinct, we measure their effect size using Cohen’s d within hallucinated regions m at the final diffusion step ($t = 0$). Samples not meeting the taxonomy criterion are re-sampled until all patches satisfy the threshold τ_{hvm} .

For **intrinsic** hallucinations, we enforce a measurement-domain violation:

$$d_{\text{meas}} = \frac{\mu_{\text{meas}}^{\text{pred}} - \mu_{\text{meas}}^{\text{gt}}}{\sigma_{\text{meas}}} \geq \tau_{\text{hvm}}. \quad (8)$$

For **extrinsic** hallucinations, we require measurement consistency but image-domain deviation:

$$\begin{cases} d_{\text{meas}} \leq \tau_{\text{hvm}}, \\ d_{\text{img}} = \frac{\mu_{\text{img}}^{\text{pred}} - \mu_{\text{img}}^{\text{gt}}}{\sigma_{\text{img}}} \geq \tau_{\text{hvm}}, \end{cases} \quad (9)$$

where $\mu_{\text{meas}}^{\text{pred}}$, $\mu_{\text{meas}}^{\text{gt}}$, $\mu_{\text{img}}^{\text{pred}}$, and $\mu_{\text{img}}^{\text{gt}}$ are masked group means, and σ_{meas} and σ_{img} are the corresponding pooled standard deviations. Cohen’s d provides a normalized effect size, making HVM domain-agnostic. τ_{hvm} controls how strictly generated samples must adhere to the taxonomy definitions.

Manifold Regularization Effect. Although gradient ascent perturbs the diffusion process, generated images remain realistic due to the diffusion prior. The denoising network μ_θ acts as a soft manifold prior, projecting samples toward high-likelihood regions of $p_{\text{data}}(x)$ in each time step. This preserves global coherence while introducing localized deviations, yielding plausible yet incorrect structures. To further enhance realism, we gradually suppress gradient ascent in the final steps, allowing the denoising prior to dominate as the process converges toward the data manifold.

Implementation Details. A key design choice is *where* to inject hallucinations. Random sampling often hits background, while segmentation-based masking needs annotations. We instead use an entropy-based strategy that selects informative regions, with patch sizes randomly drawn from 16–24 pixels to match typical hallucination extent. For each candidate patch, we compute its Shannon entropy:

$$H(p) = - \sum_i p_i \log p_i, \quad (10)$$

where p_i is the normalized intensity histogram. Patches failing the entropy or background-ratio thresholds (e.g., out-of-brain regions) are rejected and resampled. This lightweight, annotation-free heuristic reliably targets semantically meaningful regions. More details are provided in the supplementary section.

3.4. Dataset Construction

A hallucination dataset is constructed using HalluGen on 1,450 MRI slices. A diffusion model is first trained on high-quality 3T brain MR images from the Human Connectome Project (HCP) [41], each with resolution 256×256 . To emulate low-field MRI (<0.36T), following DynamicDPS [23], a composite degradation operator is applied, $\mathcal{A} = \text{Blur}(\text{DS}_k(\Gamma_\gamma(\cdot)))$, with $k = 4$ and $\gamma = 0.7$, creating a moderately ill-posed nonlinear inverse problem suitable for controlled hallucination generation.

For each ground-truth image x_{gt} , three outputs are generated: **(1)** a non-hallucinated baseline using DPS; **(2)** intrinsic hallucinations; and **(3)** extrinsic hallucinations syn-

thesized by HalluGen. Each hallucinated image contains $n \in \{1, 2, 3\}$ non-overlapping patches.

Outside masked regions are smoothly interpolated with the baseline at each diffusion timestep to confine evaluation to injected hallucinations. Each entry consists of (x_{gt}, y, \hat{x}, m) and the dataset is balanced across types (1,450 intrinsic and extrinsic cases each).

4. Experiments

4.1. Dataset Statistics

The dataset maintains balanced coverage across hallucination characteristics. Intrinsic and extrinsic samples each account for 50% of the dataset, and images with one to three hallucinated patches are evenly distributed (30–38%). Spatially, hallucinations span all four image quadrants (22–30%), ensuring diverse anatomical coverage. This balanced design supports fair benchmarking across diverse scenarios.

4.2. Validation of Generated Hallucinations

Figure 3 shows intrinsic and extrinsic hallucinations generated by HalluGen. The images appear realistic, altering tissue morphology such as sulci and ventricles. A key trend emerges: intrinsic hallucinations often cause morphological distortions (shape or size), whereas extrinsic ones introduce new plausible structures, leading to topological changes.

We assess perceptual realism using FID and semantic deviation via tissue segmentation IoU within hallucinated regions. Since no prior work addresses hallucination generation for image restoration, we compare HalluGen against three baselines: (1) vanilla DPS [10] as a non-hallucinated reference, (2) random rotation in selected patches, and (3) measurement perturbation by adding noise in measurement space (e.g., the original input image). We additionally evaluate HalluGen with different feature extractors. Gaussian Mixture Models are used for segmenting gray matter, white matter, and CSF.

Table 1 shows HalluGen achieves FID comparable to DPS, while segmentation IoU drops by 50% within hallucinated regions, indicating strong semantic deviation. Although random rotations and measurement perturbations yield low FID, they apply only to intrinsic cases and introduce patch artifacts. HalluGen performs consistently across different feature extractors; additional visuals are provided in the supplementary. An expert study ($n=2$), where HalluGen outputs were mixed with vanilla DPS reconstructions, yielded only 50.5% identification accuracy, confirming that HalluGen produces visually realistic hallucinations.

We validate HalluGen’s taxonomy compliance in Tab. 2 by measuring measurement- and image-space deviations within masked regions. Intrinsic hallucinations exhibit measurement loss roughly 7 times higher than DPS, confirming violation of measurement consistency. Extrinsic

Table 1. **Comparisons of perceptual realism and semantic deviation of HalluGen and other baselines.** For HalluGen, FID is low, comparable to DPS, confirming realism, while segmentation IoU within hallucinated regions drops sharply across different feature extractors, verifying semantic deviation.

Method	FID ↓	IoU ↓	Tax. Comp.
DPS [10]	0.32	0.861±0.09	-
Random Rotation	0.32	0.393±0.12	Intr. only
Meas. Perturb.	0.48	0.721±0.10	Intr. only
HalluGen + MedSAM [9]	0.41	0.363±0.15	Both
HalluGen + SAM [24]	0.36	0.367±0.15	Both
HalluGen + DINOv3 [40]	0.43	0.362±0.04	Both

hallucinations retain low measurement loss but diverge in image space, consistent with the formal taxonomy (Eq. 2–3). Fig. 3 further visualizes measurement-space difference maps, with extrinsic cases showing much lower errors than intrinsic ones within hallucinated regions.

Table 2. **Hallucination taxonomy compliance of HalluGen using Mean Squared Error within masked region.** Intrinsic sustains high measurement loss while extrinsic maintains low measurement loss despite semantic errors in image space. This validation confirms HalluGen faithfully generates both taxonomy types.

Predicted Region	Meas. Loss	Image Loss
DPS	0.006	0.022
Intrinsic	0.039	0.058
Extrinsic	0.003	0.041

4.3. Controllability of HalluGen

HalluGen enables fine-grained control over hallucination characteristics. We validate controllability along three dimensions: gradient strength, patch count, and patch size. We focus on intrinsic hallucinations, as extrinsic generation involves balancing multiple loss terms that complicate the isolation of individual control factors.

Severity control via gradient strength. Figure 4 (left) shows that hallucination severity increases with gradient ascent strength, γ . The squared error in hallucinated regions increases from 718 ($\gamma = 0.0005$) to 767 ($\gamma = 0.01$), showing that stronger gradients induce more severe, measurement-inconsistent hallucinations. FID remains stable, indicating preserved perceptual realism.

Spatial scalability via number of patches. Figure 4 (middle) validates that HalluGen scales with the number of patches. As the number increases from 1 to 5, total squared error grows approximately linearly (150 to 810). FID remains consistently low, confirming that distributed hallucinations maintain realistic appearances.

Patch size flexibility. Figure 4 (right) shows controllability across different spatial granularities. Squared error scales with patch area (16×16: 488, 64×64: 9000), while FID remains stable, demonstrating consistent realism across

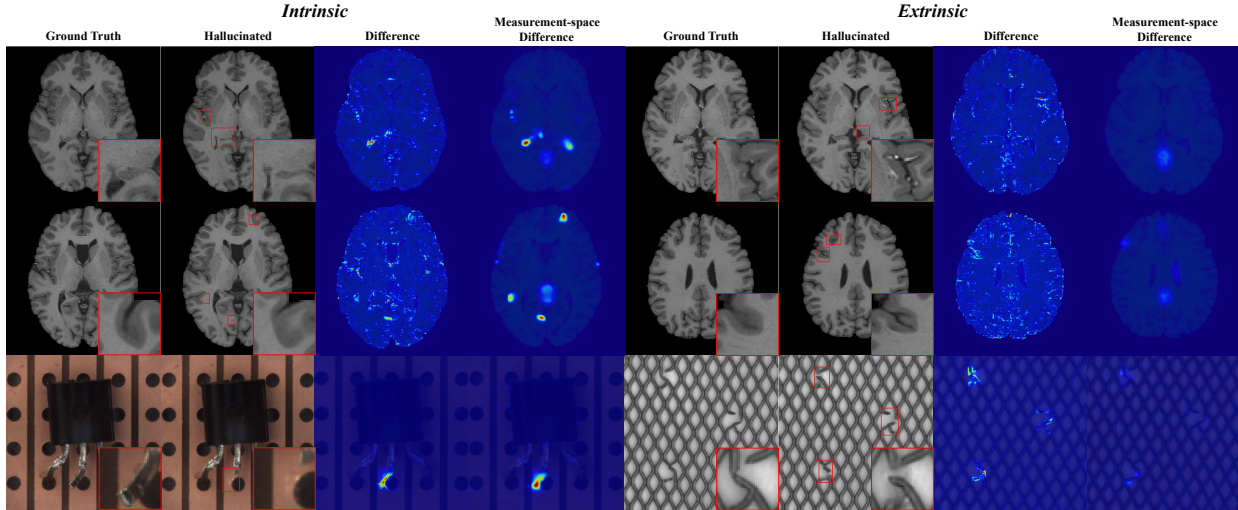


Figure 3. **Representative hallucinations generated by HalluGen across domains.** Top: Controlled synthesis of intrinsic and extrinsic hallucinations in our open dataset for MR images. Bottom: Cross-domain generalization to industrial imagery (MVTEC AD). HalluGen produces realistic yet semantically incorrect features across domains. More visual results are in the supplementary.

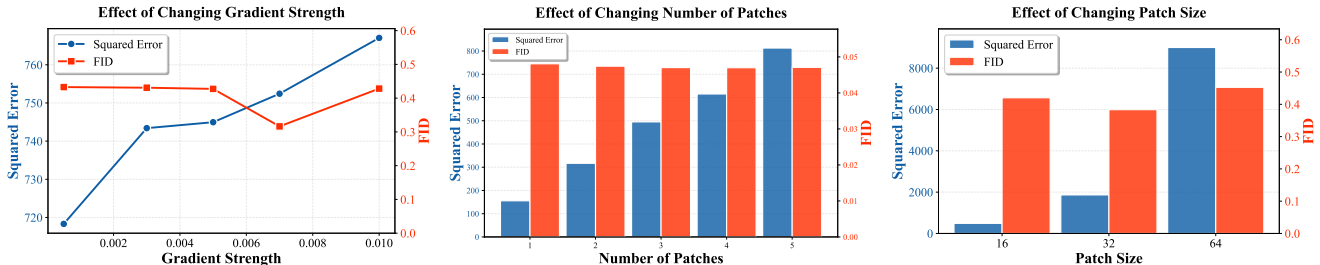


Figure 4. **Controllability of HalluGen.** Left: Severity increases with gradient strength γ . Middle: Severity scales linearly with number of patches while FID stays low. Right: Stable realism across patch sizes (16×16 – 64×64). HalluGen provides fine-grained control over severity, spatial extent, and granularity while preserving realism.

fine-grained and coarse spatial scales.

These results show that HalluGen enables precise control over hallucination severity, extent, and scale while preserving perceptual realism through manifold regularization.

4.4. Cross-Domain and Cross-Task Generalization

We evaluate HalluGen’s generalizability by sampling 200 images per domain-task pair (1600 total) for both intrinsic and extrinsic, summarized in Fig. 6. For MVTEC AD [5], semantic deviation is measured by the change in anomaly scores between ground-truth and generated images using the pre-trained PatchCore [37]. On ImageNet [12], it is quantified by the CLIP score, the distance between CLIP embeddings of the ground-truth and generated images.

Fig. 3 shows HalluGen generating hallucinated features on MVTEC AD, such as missing transistor legs and distorted grid patterns. It maintains low FID with large change in anomaly score (Fig. 6), indicating perceptually plausible but semantically divergent outputs. HalluGen also generalizes to natural images, generating realistic distortions such as extra insect legs, warped tires with an increase in CLIP score

compared to DPS (Figs. 5, 6).

Additional experiments on HCP [41] confirm robustness across standard restoration tasks, including super-resolution and deblurring, showing that HalluGen generalizes across both domains and restoration types.

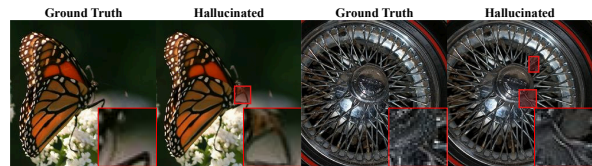


Figure 5. **Visual results of HalluGen on ImageNet.** HalluGen generalizes beyond safety-critical domains and can generate realistic hallucinated features as highlighted in red boxes.

4.5. Case Study I: Hallucination Metric Benchmark

The evaluation of hallucination has been hindered by the lack of labeled data. Leveraging HalluGen-generated dataset, we establish the first benchmark for evaluating hallucination sensitivity of full-reference image quality met-

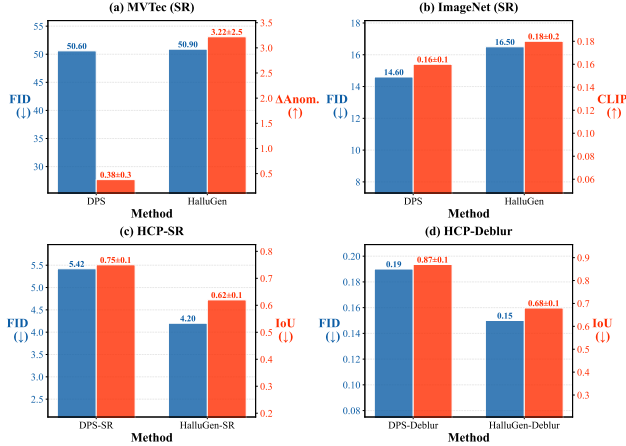


Figure 6. **Cross-domain and cross-task generalization of HalluGen.** Low FID and high semantic deviations confirm HalluGen’s generalizability. For SR, we use $\times 6$; for deblur, $\sigma = 3.0$.

rics. We assess representative metrics by discriminability (Cohen’s d), detectability (AUC-ROC), sharpness bias curve (SBC), and correlation with hallucination severity (Spearman’s ρ). SBC is computed as the area under the win-rate curve obtained by progressively low-pass filtering non-hallucinated images. Severity is defined as the sum of squared error within hallucinated regions scaled by the number of hallucinated patches, to penalize images with more frequent hallucination occurrences.

We also develop a hallucination-aware baseline, *Semantic Hallucination Assessment via Feature Evaluation (SHAFE)*, to address the limitation of conventional metrics on hallucinations and evaluate it alongside existing metrics.

Semantic Hallucination Assessment via Feature Evaluation (SHAFE). Most full-reference metrics use uniform averaging over errors, which suppresses hallucinations that are *localized and sparse*. SHAFE applies soft attention-based aggregation [49], emphasizing rare but structurally inconsistent regions while preserving global context. Given a prediction \hat{x} and ground truth x_{gt} , SHAFE is computed as follows:

- **Patch-level feature discrepancy.** A low-pass filter is applied to both inputs to suppress high-frequency noise and emphasize structural content. Each image is then fed into a pretrained vision encoder to extract semantic features, and cosine distance δ_{cos} is computed for each patch. Shallow multi-layer features are extracted to retain spatial richness and reduce dataset-specific bias of the encoder.

- **Softmax-based aggregation.** These patch scores are then aggregated using temperature-controlled softmax:

$$\text{SHAFE} = \sum_i w_i \delta_{cos,i}, \quad w_i = \frac{\exp(\delta_{cos,i}/\tau)}{\sum_j \exp(\delta_{cos,j}/\tau)}. \quad (11)$$

Smaller τ assigns exponentially greater weights, w_i , to lo-

cal and severe errors. Its patch-based design enables hallucination localization, with Fig. 7 showing SHAFE heatmaps accurately highlighting real failure regions.

SHAFE operates in feature space, but its formulation is general and can be applied to other metrics. Moreover, its differentiability allows integration into supervised training pipelines, opening avenues for future extensions toward hallucination-aware model optimization. See the supplementary material for more details.

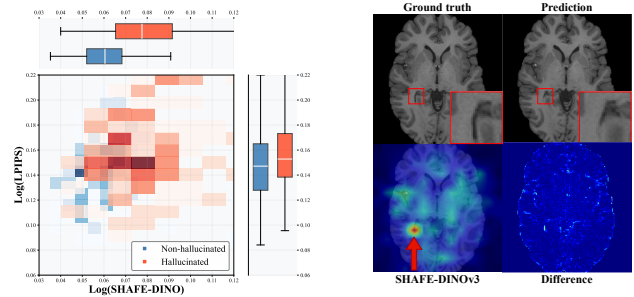


Figure 7. **Bivariate distributions of SHAFE-DINOv3 vs. LPIPS (left) and Spatial localization ability of SHAFE on real prediction (right).** Hallucinated examples shift toward higher SHAFE values, indicating improved separability compared to LPIPS.

Perceptual metrics are insensitive to hallucinations; Tab. 3 summarizes the performance of the metrics on hallucination. LPIPS and DISTs perform marginally above chance in hallucination detection, showing limited sensitivity. Their *low* Cohen’s $|d|$ and *high* per-sample variability reveal inconsistent responses across hallucinations, making them unreliable indicators. Because they uniformly average spatial errors and rely on ImageNet-trained features, these metrics favor perceptual sharpness over semantic correctness and often overlook structurally inconsistent regions.

Multi-scale improves sensitivity. MS-SSIM substantially improves hallucination sensitivity over SSIM, benefiting from its multi-scale formulation that captures hallucinations of varying sizes. This demonstrates the value of incorporating multi-scale information for more reliable image evaluation. However, it still underperforms SHAFE due to its uniform aggregation strategy.

Pixel metrics show type-dependent performance. Pixel-based metrics achieve moderate detection on intrinsic hallucinations that violate measurement consistency and produce large pixel-space deviations. However, their performance degrades substantially on extrinsic cases that remain measurement-consistent despite semantic incorrectness, limiting their utility for comprehensive evaluation.

SHAFE achieves superior performance. SHAFE variants outperform baselines, with *all feature backbones* improving all benchmark metrics by 30% over the best baselines. Especially, SHAFE-ResNet50 outperforms LPIPS and DISTs, despite sharing the same pre-training domain,

Table 3. **Comprehensive hallucination benchmark across metrics.** Comparison of pixel- and feature-based metrics on effect size (discrimination), AUC (detection), Sharpness Bias Curve (sharpness bias), and severity correlation (spearman rank correlation). The rightmost column shows AUC on raw predictions with manually labeled (binary) hallucinations. Baseline metrics show weak hallucination sensitivity, whereas SHAFE improve detection and interpretability. FPR/FNR are calculated using the optimal threshold from AUC curve.

Metric	Type	Effect Size (Cohen’s $ d $) \uparrow		AUC-ROC \uparrow		SBC \uparrow		Severity (ρ) \uparrow		FNR/FPR (%) \downarrow	Real AUC \uparrow
		Intr.	Extr.	Intr.	Extr.	Intr.	Extr.	Intr.	Extr.		
PSNR	Pixel	0.33 \pm 0.95	0.02 \pm 0.99	0.59	0.51	0.76	0.49	0.37	0.32	62 / 28	0.58
SSIM	Pixel	0.09 \pm 0.99	0.33 \pm 1.03	0.52	0.40	0.22	0.08	0.11	-0.17	99 / 0	0.53
MS-SSIM [47]	Pixel	0.69 \pm 1.00	0.16 \pm 0.99	0.79	0.21	0.84	0.27	0.43	0.08	36 / 57	0.57
SCC [53]	Pixel	0.06 \pm 1.03	0.16 \pm 1.01	0.48	0.46	0.23	0.12	0.05	0.02	80 / 18	0.47
LPIPS [52]	Feature	0.03 \pm 1.00	0.01 \pm 0.99	0.51	0.50	0.14	0.12	0.11	0.14	26 / 70	0.42
DISTS [13]	Feature	0.06 \pm 0.99	0.10 \pm 0.99	0.52	0.54	0.27	0.27	0.19	0.12	31 / 60	0.44
VIF [39]	Pixel	0.29 \pm 1.00	0.00 \pm 0.99	0.58	0.50	0.28	0.11	0.27	0.17	42 / 48	0.47
SHAFE-ResNet50 [51]	Feature	1.18\pm1.12	0.84 \pm 1.28	0.82	0.72	0.79	0.71	0.51	0.57	27 / 25	0.58
SHAFE-MedSAM [9]	Feature	1.13 \pm 1.26	0.93\pm1.34	0.81	0.75	0.77	0.71	0.47	0.60	32 / 14	0.70
SHAFE-DINOv3 [40]	Feature	1.12 \pm 1.17	0.92 \pm 1.30	0.76	0.74	0.71	0.67	0.51	0.58	30 / 26	0.79

highlighting the effectiveness of our weighted aggregation to emphasize local failures. Moreover, all SHAFE variants exhibit low sharpness bias, confirming that the combination of low-pass filtering and our multi-layer feature extraction strategy reduces the reliance on high-frequency artifacts.

We evaluated metrics on real restoration outputs by annotating 300 predictions from SwinIR [30], EDSR [31], and ESRGAN [44]. SHAFE shows much stronger discrimination, improving AUC by 0.2 over traditional metrics (Table 3), aligning more closely with human judgment. Figure 7 shows that SHAFE provides distinctly better separation between images with and without hallucinations than LPIPS, demonstrating its robustness in real cases.

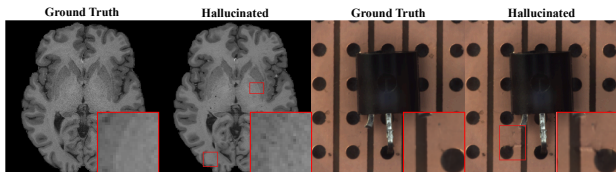


Figure 8. **Failure case of HalluGen in homogeneous regions.** In smooth regions (e.g., brain putamen or background), diffusion prior dominates, leading to visually weak hallucinations.

4.6. Case Study II: Hallucination Detection

HalluGen’s utility can be extended to developing data-driven hallucination detector. We train a *reference-free hallucination detector* using a CNN that takes the prediction \hat{x} and measurement y as input and predicts whether hallucinations are present, without requiring ground-truth images. The model is trained on the full HalluGen dataset (4,350 images) and evaluated on: (1) a held-out HalluGen split (702 images; evenly balanced across intrinsic, extrinsic, and non-hallucinated cases), and (2) same real restoration outputs used in the benchmark in Tab. 3.

As shown in Table 4, the detector achieves strong performance on synthetic data and generalizes to real predictions,

despite its simple architecture. Detection is notably easier for intrinsic hallucinations than extrinsic by AUC \approx 0.14. This is because intrinsic hallucinations break measurement consistency, whereas extrinsic ones remain consistent with y and are therefore harder to identify. Overall, these results show that HalluGen *transfers to real model failures* and enables comprehensive, systematic hallucination evaluation that was previously infeasible.

Table 4. **Reference-free hallucination detection.** CNN trained only on HalluGen; thresholds selected on validation.

Test Set	AUC \uparrow	F1 \uparrow
HalluGen (Intrinsic)	0.91	0.95
HalluGen (Extrinsic)	0.77	0.76
Real Predictions	0.73	0.63

5. Conclusion

We present *HalluGen*, a principled framework for controllable hallucination synthesis, and construct the first hallucination dataset for image restoration with patch-level annotations. We demonstrate HalluGen’s utility in two key applications: (1) establishing a hallucination-metric benchmark that reveals the failure of existing image quality metrics and developing *SHAFE*, which improves hallucination sensitivity via soft-attention pooling over feature errors; and (2) training reference-free hallucination detectors that generalize to real restoration outputs. These results demonstrate that *HalluGen transfers to real model failures, enabling systematic study of hallucinations in real-world settings*. HalluGen has several limitations, including difficulty inducing hallucinations in homogeneous regions due to strong diffusion priors (Fig. 11) and lack of explicit semantic control. The current dataset is restricted to MR images, and extending HalluGen to other safety-critical domains remains an important direction. Nevertheless, HalluGen establishes the first systematic foundation for generating, detecting, and evaluating hallucinations in image restoration. We release

our code, dataset, and metrics to support further research and safer deployment in safety-critical domains.

References

- [1] Mahmoud Afifi. 11k hands: gender recognition and biometric identification using a large dataset of hand images. *Multimedia Tools and Applications*, 78(15):20835–20854, 2019. 1
- [2] Sumukh K Aithal, Pratyush Maini, Zachary Chase Lipton, and J Zico Kolter. Understanding hallucinations in diffusion models through mode interpolation. In *The Thirty-eighth Annual Conference on Neural Information Processing Systems*, 2024. 1, 2
- [3] Daniel C. Alexander, Zikic Darko, Aurobrata Ghosh, Ryutaro Tanno, Viktor Wottschel, et al. Image quality transfer and applications in diffusion mri. *NeuroImage*, 152:283–298, 2017. 2
- [4] Yejin Bang, Ziwei Ji, Alan Schelten, Anthony Hartshorn, Tara Fowler, Cheng Zhang, Nicola Cancedda, and Pascale Fung. Hallulens: Llm hallucination benchmark. 2025. 3
- [5] Paul Bergmann, Michael Fauser, David Sattlegger, and Carsten Steger. Mvtec ad – a comprehensive real-world dataset for unsupervised anomaly detection. In *IEEE/CVF Conference on Computer Vision and Pattern Recognition (CVPR)*, 2019. 1, 3, 6
- [6] S. Bhadra, V. A. Kelkar, F. J. Brooks, and M. A. Anastasio. On hallucinations in tomographic image reconstruction. *IEEE Transactions on Medical Imaging*, 40(11):3249–3260, 2021. 1, 2, 3
- [7] Yochai Blau and Tomer Michaeli. The perception-distortion tradeoff. In *The IEEE / CVF Computer Vision and Pattern Recognition Conference (CVPR)*, 2018. 2
- [8] Xiangyu Chen, Xintao Wang, Jiantao Zhou, Yu Qiao, and Chao Dong. Activating more pixels in image super-resolution transformer. In *Proceedings of the IEEE/CVF Conference on Computer Vision and Pattern Recognition (CVPR)*, 2023. 1, 2
- [9] Junlong Cheng, Jin Ye, Zhongying Deng, Jianpin Chen, Tianbin Li, Haoyu Wang, Yanzhou Su, Ziyang Huang, Jilong Chen, Lei Jiangand Hui Sun, Junjun He, Shaoting Zhang, Min Zhu, and Yu Qiao. Sam-med2d, 2023. 4, 5, 8, 1
- [10] Hyungjin Chung, Jeongsol Kim, Michael Thompson McCann, Marc Louis Klasky, and Jong Chul Ye. Diffusion posterior sampling for general noisy inverse problems. In *The Eleventh International Conference on Learning Representations*, 2023. 1, 2, 3, 5
- [11] Hyungjin Chung, Dohoon Ryu, Michael T McCann, Marc L Klasky, and Jong Chul Ye. Solving 3d inverse problems using pre-trained 2d diffusion models. In *IEEE/CVF Conference on Computer Vision and Pattern Recognition*, 2023. 2
- [12] Jia Deng, Wei Dong, Richard Socher, Li-Jia Li, Kai Li, and Li Fei-Fei. Imagenet: A large-scale hierarchical image database. In *IEEE Conference on Computer Vision and Pattern Recognition (CVPR)*, 2009. 1, 6
- [13] Keyan Ding, Kede Ma, Shiqi Wang, and Eero P. Simoncelli. Image quality assessment: Unifying structure and texture similarity. *CoRR*, 2020. 2, 8
- [14] Chao Dong, Chen Change Loy, Kaiming He, and Xiaoou Tang. Learning a deep convolutional network for image super-resolution. In *European Conference on Computer Vision (ECCV)*, 2014. 2
- [15] Karthik Gopinath, Andrew Hoopes, Daniel C. Alexander, Steven E. Arnold, Yael Balbastre, et al. Synthetic data in generalizable, learning-based neuroimaging. *Imaging Neuroscience*, 2:1–22, 2024. 2
- [16] Tianrui Guan, Fuxiao Liu, Xiyang Wu, Ruiqi Xian, Zongxia Li, Xiaoyu Liu, Xijun Wang, Lichang Chen, Furong Huang, Yaser Yacoub, Dinesh Manocha, and Tianyi Zhou. Hallusionbench: An advanced diagnostic suite for entangled language hallucination and visual illusion in large vision-language models. In *Proceedings of the IEEE/CVF Conference on Computer Vision and Pattern Recognition (CVPR)*, 2024. 3
- [17] Jonathan Ho, Ajay Jain, and Pieter Abbeel. Denoising diffusion probabilistic models. In *Advances in Neural Information Processing Systems*, 2020. 3, 1
- [18] Juan E. Iglesias, Benjamin Billot, Yaël Balbastre, Colin Magdamo, Steven E. Arnold, et al. Synthsr: A public ai tool to turn heterogeneous clinical brain scans into high-resolution t1-weighted images for 3d morphometry. *Science Advances*, 9(5), 2023. 2
- [19] Chaoya Jiang, Hongrui Jia, Mengfan Dong, Wei Ye, Haiyang Xu, Ming Yan, Ji Zhang, and Shikun Zhang. Hal-eval: A universal and fine-grained hallucination evaluation framework for large vision language models. In *Proceedings of the 32nd ACM International Conference on Multimedia*, 2024. 3
- [20] Bahjat Kawar, Michael Elad, Stefano Ermon, and Jiaming Song. Denoising diffusion restoration models. In *Advances in Neural Information Processing Systems*, 2022. 2
- [21] Seunghoi Kim, Henry FJ Tregidgo, Ahmed K Eldaly, Matteo Figini, and Daniel C Alexander. A 3d conditional diffusion model for image quality transfer—an application to low-field mri. *arXiv preprint arXiv:2311.06631*, 2023. 1
- [22] Seunghoi Kim, Chen Jin, Tom Diethe, Matteo Figini, Henry F. J. Tregidgo, et al. Tackling structural hallucination in image translation with local diffusion. In *European Conference on Computer Vision (ECCV)*, 2024. 2, 1
- [23] Seunghoi Kim, Henry F. J. Tregidgo, Matteo Figini, Chen Jin, Sarang Joshi, and Daniel C. Alexander. Tackling Hallucination from Conditional Models for Medical Image Reconstruction with DynamicDPS . In *proceedings of Medical Image Computing and Computer Assisted Intervention – MICCAI*, 2025. 1, 2, 3, 4
- [24] Alexander Kirillov, Eric Mintun, Nikhila Ravi, Hanzi Mao, Chloe Rolland, Laura Gustafson, Tete Xiao, Spencer Whitehead, Alexander C. Berg, Wan-Yen Lo, Piotr Dollár, and Ross Girshick. Segment anything. In *2023 IEEE/CVF International Conference on Computer Vision (ICCV)*, 2023. 4, 5
- [25] Orest Kupyn, Volodymyr Budzan, Mykola Mykhailych, Dmytro Mishkin, and Jiri Matas. DeblurGAN: Blind Motion Deblurring Using Conditional Adversarial Networks . In *IEEE/CVF Conference on Computer Vision and Pattern Recognition (CVPR)*, 2018. 1

- [26] Vick Lau, Linfang Xiao, Yujiao Zhao, Shi Su, Ye Ding, et al. Pushing the limits of low-cost ultra-low-field mri by dual-acquisition deep learning 3d superresolution. *Magnetic Resonance in Medicine*, 90(2):400–416, 2023. 2
- [27] Y. Lecun, L. Bottou, Y. Bengio, and P. Haffner. Gradient-based learning applied to document recognition. *Proceedings of the IEEE*, 86(11):2278–2324, 1998. 1
- [28] Junyi Li, Xiaoxue Cheng, Wayne Xin Zhao, Jian-Yun Nie, and Ji-Rong Wen. Halueval: A large-scale hallucination evaluation benchmark for large language models, 2023. 3
- [29] Yifan Li, Yifan Du, Kun Zhou, Jinpeng Wang, Xin Zhao, and Ji-Rong Wen. Evaluating object hallucination in large vision-language models. In *Proceedings of the Conference on Empirical Methods in Natural Language Processing*, 2023. 3
- [30] Jingyun Liang, Jiezhong Cao, Guolei Sun, Kai Zhang, Luc Van Gool, and Radu Timofte. Swinir: Image restoration using swin transformer. *arXiv preprint arXiv:2108.10257*, 2021. 1, 2, 8, 5
- [31] Bee Lim, Sanghyun Son, Heewon Kim, Seungjun Nah, and Kyoung Mu Lee. Enhanced deep residual networks for single image super-resolution. In *The IEEE Conference on Computer Vision and Pattern Recognition (CVPR) Workshops*, 2017. 1, 2, 8
- [32] Hongxiang Lin, Matteo Figini, Felice D’Arco, Godwin Ogbale, Ryutaro Tanno, et al. Low-field magnetic resonance image enhancement via stochastic image quality transfer. *Medical Image Analysis*, 87:102807, 2023. 2
- [33] B. H. Menze, A. Jakab, S. Bauer, et al. The multimodal brain tumor image segmentation benchmark (brats). *IEEE Transactions on Medical Imaging*, 2015. 3
- [34] Trevine Oorloff, Yaser Yacoob, and Abhinav Shrivastava. Mitigating hallucinations in diffusion models through adaptive attention modulation. *arXiv preprint arXiv:2502.16872*, 2025. 1, 2
- [35] Eunkyung Park, Minyeong Kim, and Gunhee Kim. Halloc: Token-level localization of hallucinations for vision language models. In *IEEE/CVF Conference on Computer Vision and Pattern Recognition (CVPR)*, 2025. 3
- [36] Mengwei Ren, Mauricio Delbracio, Hossein Talebi, Guido Gerig, and Peyman Milanfar. Multiscale structure guided diffusion for image deblurring. In *IEEE/CVF International Conference on Computer Vision (ICCV)*, pages 10687–10699, 2023. 1
- [37] Karsten Roth, Latha Pemula, Joaquin Zepeda, Bernhard Schölkopf, Thomas Brox, and Peter Gehler. Towards total recall in industrial anomaly detection. In *Proceedings of the IEEE/CVF Conference on Computer Vision and Pattern Recognition*, pages 14298–14308, 2022. 6
- [38] L Rout, Y Chen, A Kumar, C Caramanis, S Shakkottai, and W Chu. Beyond first-order tweedie: Solving inverse problems using latent diffusion, 2024. 2
- [39] H.R. Sheikh and A.C. Bovik. Image information and visual quality. *IEEE Transactions on Image Processing*, 15(2):430–444, 2006. 2, 8
- [40] Oriane Siméoni, Huy V. Vo, Maximilian Seitzer, Federico Baldassarre, Maxime Oquab, Cijo Jose, Vasil Khalidov, Marc Szafraniec, Seungeun Yi, Michaël Ramamonjisoa, Francisco Massa, Daniel Haziza, Luca Wehrstedt, Jianyuan Wang, Timothée Darcet, Théo Moutakanni, Leonel Sentana, Claire Roberts, Andrea Vedaldi, Jamie Tolan, John Brandt, Camille Couprie, Julien Mairal, Hervé Jégou, Patrick Labatut, and Piotr Bojanowski. DINOv3, 2025. 4, 5, 8
- [41] Stamatios N. Sotiropoulos, Saâd Jbabdi, Junqian Xu, Jesper L. R. Andersson, Steen Moeller, et al. Advances in diffusion mri acquisition and processing in the human connectome project. *NeuroImage*, 80:125–143, 2013. 1, 4, 6, 3
- [42] Matthieu Terris, Samuel Hurault, Maxime Song, and Julián Tachella. Reconstruct anything model: a lightweight foundational model for computational imaging. *arXiv preprint arXiv:2503.08915*, 2025. 2
- [43] Matthew Tivnan, Siyeop Yoon, Zhenhong Chen, Xiang Li, Dufan Wu, et al. Hallucination Index: An Image Quality Metric for Generative Reconstruction Models. In *Proceedings of Medical Image Computing and Computer Assisted Intervention – MICCAI*, 2024. 2
- [44] Xintao Wang, Ke Yu, Shixiang Wu, Jinjin Gu, Yihao Liu, et al. Esrgan: Enhanced super-resolution generative adversarial networks. In *The European Conference on Computer Vision Workshops (ECCVW)*, 2018. 1, 2, 8, 5
- [45] Yinhuai Wang, Jiwen Yu, and Jian Zhang. Zero-shot image restoration using denoising diffusion null-space model. *The Eleventh International Conference on Learning Representations*, 2023. 2
- [46] Yuxuan Wang, Yueqian Wang, Dongyan Zhao, Cihang Xie, and Zilong Zheng. Videohalluciner: Evaluating intrinsic and extrinsic hallucinations in large video-language models. *arxiv*, 2024. 3
- [47] Z. Wang, E.P. Simoncelli, and A.C. Bovik. Multiscale structural similarity for image quality assessment. In *The Thirty-Seventh Asilomar Conference on Signals, Systems & Computers*, 2003. 2, 8
- [48] Xiyang Wu, Tianrui Guan, Dianqi Li, Shuaiyi Huang, Xiaoyu Liu, Xijun Wang, Ruiqi Xian, Abhinav Shrivastava, Furong Huang, Jordan Lee Boyd-Graber, Tianyi Zhou, and Dinesh Manocha. Autohallusion: Automatic generation of hallucination benchmarks for vision-language models, 2024. 3
- [49] Wenpeng Yin, Hinrich Schütze, Bing Xiang, and Bowen Zhou. ABCNN: Attention-based convolutional neural network for modeling sentence pairs. *Transactions of the Association for Computational Linguistics*, 4:259–272, 2016. 7, 4
- [50] Bingliang Zhang, Wenda Chu, Julius Berner, Chenlin Meng, Anima Anandkumar, and Yang Song. Improving diffusion inverse problem solving with decoupled noise annealing, 2024. 2
- [51] Richard Zhang. Making convolutional networks shift-invariant again. In *International Conference on Machine Learning (ICML)*, 2019. 8, 4
- [52] Richard Zhang, Phillip Isola, Alexei A Efros, Eli Shechtman, and Oliver Wang. The unreasonable effectiveness of deep features as a perceptual metric. In *Proceedings of the IEEE/CVF Conference on Computer Vision and Pattern Recognition (CVPR)*, 2018. 1, 2, 8

- [53] J. Zhou, D. L. Civco, and J. A. Silander. A wavelet transform method to merge landsat tm and spot panchromatic data. *International Journal of Remote Sensing*, 19(4):743–757, 1998. [2](#), [8](#)
- [54] Yuanzhi Zhu, Kai Zhang, Jingyun Liang, Jiezhong Cao, Bihan Wen, et al. Denoising diffusion models for plug-and-play image restoration. In *IEEE Conference on Computer Vision and Pattern Recognition Workshops (NTIRE)*, 2023. [2](#)

HalluGen: Synthesizing Realistic and Controllable Hallucinations for Evaluating Image Restoration

Supplementary Material

Table of Contents

- **6. HalluGen**
 - Sec. 6.1 Implementation Details
 - Sec. 6.2 Ablations
 - Sec. 6.3 Qualitative Results
- **7. Dataset**
 - Sec. 7.1 Instructions for Dataset
 - Sec. 7.2 Computational Cost
 - Sec. 7.3 Limitations
 - Sec. 7.4 License and Ethics Statement
- **8. SHAFE**
 - Sec. 8.1 Implementation Details
 - Sec. 8.2 Ablations
 - Sec. 8.3 Localization Results
 - Sec. 8.4 Limitations of SHAFE
 - Sec. 8.5 Inference Speed
- **9. Hallucination Detectors**
- **Figures**
 - Fig. 9: Effect of temperature τ in softmax aggregation for SHAFE (AUC vs. τ)
 - Fig. 10: Visual results of SHAFE heatmap on both HalluGen and real restoration outputs
 - Fig. 11: Visual examples of SHAFE limitations
 - Fig. 12: Inference time comparison for baseline metrics vs. SHAFE-ResNet50
 - Fig. 13: Network architecture of reference-free hallucination detector
 - Fig. 14: Visual results of HalluGen on brain MRI
 - Fig. 15: Visual results of HalluGen on MVTEC AD
 - Fig. 16: Visual results of HalluGen on ImageNet
- **Tables**
 - Tab. 5: HalluGen ablations using mean squared error within masked region
 - Tab. 6: SHAFE ablations using AUC on hallucination detection
 - Tab. 7: Impact of feature-layer selection on SHAFE hallucination detection

6. HalluGen

6.1. Implementation Details

We provide additional implementation details for HalluGen. Intrinsic and extrinsic generation procedures are summarized in Algo. 1 and Algo. 2. We first obtain a non-hallucinated baseline x_{base} using DPS [10], then sample candidate patches for hallucination injection. Patches failing entropy or background thresholds are rejected and re-

sampled. HalluGen is initialized either from Gaussian noise (when $t_{\text{skip}} = \text{None}$) or from a partially noised version of x_{base} at timestep t_{skip} .

At each reverse step, we compute the Tweedie estimate $\hat{x}_0(x_t)$. When interpolation is enabled, $\hat{x}_0(x_t)$ is blended with x_{base} outside the mask to preserve fidelity in non-masked regions. Intrinsic generation modifies only the measurement-consistency term, whereas extrinsic additionally applies a feature-space loss.

To maintain realism and avoid patch artifacts, all ascent weights are set to zero after timestep t_{stop} , following LocalDiffusion [22], allowing the diffusion prior to refine boundaries in later steps. Finally, the Hallucination Verification Module (HVM) checks whether masked deviations satisfy the taxonomy criteria (Eqs. 2, 3) via Cohen’s d ; samples failing the threshold τ_{hvm} are rejected and regenerated.

Hyperparameters. We use the following default settings:

- Diffusion solver: DDPM [17]
- Diffusion parameterization: ε_θ
- Diffusion steps: $T = 1000$
- Skip timestep: $t_{\text{skip}} = 200$
- Measurement-consistency weight: $\lambda_t = 1.0$
- Intrinsic ascent weight: $\gamma_t = 0.002$
- Extrinsic ascent weights: $\gamma_{1,t}, \gamma_{2,t} = 0.007$
- Feature-loss encoder: MedSAM [9]
- Entropy / background thresholds: 1.4/0.05
- HVM threshold: $\tau_{\text{hvm}} = 0.1$
- Patch size: 16–24
- Number of patches: 1–3
- Ascent cut-off timestep: $t_{\text{stop}} = 10$

6.2. Ablations

In this section, we ablate each HalluGen component: HVM, entropy-based patch selection, and the feature-space loss.

HVM maximizes hallucination while adhering to hallucination taxonomy. HVM enforces the intrinsic/extrinsic definitions in Equations 2 and 3 by rejecting samples that do not exhibit sufficient deviation in masked regions. As shown in Tab. 5, enabling HVM increases measurement- and image-space losses for intrinsic cases by roughly 7% and 20%, indicating stronger violations of data fidelity as required. For extrinsic cases, HVM lowers measurement-space error while increasing image-space deviation by over 56%, enforcing larger semantic changes while more strictly preserving measurement consistency. These results confirm that HVM improves taxonomy compliance by pushing intrinsic hallucinations toward greater measurement inconsis-

Algorithm 1 HalluGen – Intrinsic Hallucination

Require: Ground truth x_{gt} , measurement y , forward operator $\mathcal{A}(\cdot)$
Require: Diffusion model μ_θ , step size $\{\lambda_t\}$, $\{\gamma_t\}$
Require: Non-hallucinated baseline x_{base}
Require: Optional skip timestep t_{skip} (or None), ascent cutoff timestep t_{stop}
Require: Interpolation flag $\text{interp} \in \{\text{true}, \text{false}\}$, interpolation schedule w_t

- 1: Sample hallucination mask $m \in \{0, 1\}^{H \times W}$ by entropy-based patch selection
- 2: **if** t_{skip} is None **then**
- 3: $t_{\text{start}} \leftarrow T$
- 4: Sample $x_T \sim \mathcal{N}(0, I)$
- 5: **else**
- 6: $t_{\text{start}} \leftarrow t_{\text{skip}}$
- 7: Sample $x_{t_{\text{start}}} \sim q(x_{t_{\text{start}}} | x_{\text{base}})$ \triangleright forward process x_{base}
- 8: **end if**
- 9: **for** $t = t_{\text{start}}, t_{\text{start}} - 1, \dots, 1$ **do**
- 10: Compute Tweedie estimate $\hat{x}_0(x_t)$
- 11: **if** $\text{interp} = \text{true}$ **then**
- 12: $\hat{x}_0(x_t) \leftarrow (1 - m) \odot [w_t \hat{x}_0(x_t) + (1 - w_t) x_{\text{base}}] + m \odot \hat{x}_0(x_t)$
- 13: **end if**
- 14: $x_{t-1} \leftarrow \mu_\theta(x_t, t) - \lambda_t \nabla_{x_t} \|(1 - m) \odot (y - \mathcal{A}(\hat{x}_0))\|_2^2$
- 15: **if** $t > t_{\text{stop}}$ **then**
- 16: $\gamma_t^{\text{eff}} \leftarrow \gamma_t$
- 17: **else**
- 18: $\gamma_t^{\text{eff}} \leftarrow 0$ \triangleright turn off ascent near the end
- 19: **end if**
- 20: $x_{t-1} \leftarrow x_{t-1} + \gamma_t^{\text{eff}} \nabla_{x_t} \|m \odot (y - \mathcal{A}(\hat{x}_0))\|_2^2 + \sigma_t \varepsilon$
- 21: **end for**
- 22: $\hat{x} \leftarrow \hat{x}_0(x_0)$
- 23: Compute d_{meas} using Eq. 8; if taxonomy constraints are not satisfied, resample m and repeat
- 24: **return** intrinsic hallucinated image \hat{x} and mask m

tency and extrinsic hallucinations toward targeted semantic deviation under measurement constraints.

Entropy-based patch selection and feature loss increase semantic deviations. The entropy-based patch selection module and the feature loss are designed to target semantically informative, hallucination-prone regions and to ensure that extrinsic hallucinations alter higher-level semantic content rather than only low-level pixel intensities. In Tab.5, removing entropy-based selection reduces both measurement- and image-space deviations for intrinsic cases, while enabling it increases these deviations by about 70%, producing more localized and meaningful per-

Algorithm 2 HalluGen – Extrinsic Hallucination

Require: Ground truth x_{gt} , measurement y , forward operator $\mathcal{A}(\cdot)$
Require: Diffusion model μ_θ , feature extractor $F(\cdot)$
Require: Step size $\{\lambda_t\}$, $\{\gamma_{1,t}\}$, $\{\gamma_{2,t}\}$
Require: Non-hallucinated baseline x_{base}
Require: Optional skip timestep t_{skip} (or None), ascent cutoff timestep t_{stop}
Require: Interpolation flag $\text{interp} \in \{\text{true}, \text{false}\}$, interpolation schedule w_t

- 1: Sample hallucination mask $m \in \{0, 1\}^{H \times W}$ by entropy-based patch selection
- 2: **if** t_{skip} is None **then**
- 3: $t_{\text{start}} \leftarrow T$
- 4: Sample $x_T \sim \mathcal{N}(0, I)$
- 5: **else**
- 6: $t_{\text{start}} \leftarrow t_{\text{skip}}$
- 7: Sample $x_{t_{\text{start}}} \sim q(x_{t_{\text{start}}} | x_{\text{base}})$ \triangleright forward process x_{base}
- 8: **end if**
- 9: **for** $t = t_{\text{start}}, t_{\text{start}} - 1, \dots, 1$ **do**
- 10: Compute Tweedie estimate $\hat{x}_0(x_t)$
- 11: **if** $\text{interp} = \text{true}$ **then**
- 12: $\hat{x}_0(x_t) \leftarrow (1 - m) \odot [w_t \hat{x}_0(x_t) + (1 - w_t) x_{\text{base}}] + m \odot \hat{x}_0(x_t)$
- 13: **end if**
- 14: $x_{t-1} \leftarrow \mu_\theta(x_t, t) - \lambda_t \nabla_{x_t} \|y - \mathcal{A}(\hat{x}_0)\|_2^2$
- 15: **if** $t > t_{\text{stop}}$ **then**
- 16: $\gamma_{1,t}^{\text{eff}} \leftarrow \gamma_{1,t}$, $\gamma_{2,t}^{\text{eff}} \leftarrow \gamma_{2,t}$
- 17: **else**
- 18: $\gamma_{1,t}^{\text{eff}} \leftarrow 0$, $\gamma_{2,t}^{\text{eff}} \leftarrow 0$ \triangleright turn off ascent near the end
- 19: **end if**
- 20: $x_{t-1} \leftarrow x_{t-1} + \gamma_{1,t}^{\text{eff}} \nabla_{x_t} \|m \odot (\hat{x}_0 - x_{\text{gt}})\|_2^2$
- 21: $x_{t-1} \leftarrow x_{t-1} + \gamma_{2,t}^{\text{eff}} \nabla_{x_t} \|m \odot (F(\hat{x}_0) - F(x_{\text{gt}}))\|_2^2 + \sigma_t \varepsilon$
- 22: **end for**
- 23: $\hat{x} \leftarrow \hat{x}_0(x_0)$
- 24: Compute d_{meas} and d_{img} using Eq. 9; if taxonomy constraints are not satisfied, resample m and repeat
- 25: **return** extrinsic hallucinated image \hat{x} and mask m

turbations. For extrinsic cases, omitting the feature loss yields small deviations within the masked region. Including it more than doubles the image-space deviation while only slightly raising measurement-space error, which remains orders of magnitude lower than intrinsic cases. This shows that the feature loss strengthens higher-level semantic modification without compromising the strict measurement consistency required for extrinsic hallucinations.

Table 5. **Effects of HVM, Entropy-based selection and Feature loss on hallucination taxonomy compliance using mean squared error within masked region (N=250).**

Case	HVM	Ent.	Feat.	Meas.	Image
Intrinsic	x	x	x	1.5×10^{-3}	3.8×10^{-3}
Intrinsic	x	v	x	2.5×10^{-3}	6.5×10^{-3}
Intrinsic	v	v	x	3.0×10^{-3}	7.0×10^{-3}
Extrinsic	x	v	x	1.6×10^{-5}	1.5×10^{-3}
Extrinsic	x	x	v	1.7×10^{-5}	2.7×10^{-3}
Extrinsic	x	v	v	2.6×10^{-5}	3.0×10^{-3}
Extrinsic	v	v	v	2.2×10^{-5}	4.7×10^{-3}

6.3. Qualitative Results

We provide additional visual examples in Fig. 14, Fig. 15, and Fig. 16, corresponding to MRI, industrial, and natural images, respectively. For natural images, we initialize sampling from the ground-truth image rather than x_{base} to preserve fidelity outside the hallucination mask and clearly isolate the injected content. These results demonstrate that HalluGen generalizes across diverse imaging domains without modification.

6.4. Failure Case Analysis

We observed three recurring challenges during dataset construction with HalluGen.

(1) Sensitivity to regional texture and homogeneity. Hallucination severity depends on the local structure of the selected region. When masks cover smooth or homogeneous areas, the diffusion prior can dominate and suppress the gradient-ascent signal needed to induce hallucination. For extrinsic cases, such regions also shrink the effective null space of the forward operator $\mathcal{A}(\cdot)$, making semantic deviations harder to produce. These issues are largely mitigated by HVM and entropy-based patch selection, which favor more informative regions.

(2) Limited control over precise morphological changes. Because HalluGen relies on stochastic sampling, it cannot deterministically specify the exact morphology or topology of hallucinated structures. While HalluGen provides spatial control and severity modulation, it does not guarantee identical hallucination patterns across runs, suggesting future work on structure-aware hallucination priors.

(3) Diffusion prior strongly influences hallucination realism. Hallucination realism depends on the data distribution of the diffusion prior. To study this, we trained two MVTEC AD diffusion models: (i) class-specific and (ii) multi-class. With identical hyperparameters, the class-specific prior produced more coherent hallucinations, whereas the multi-class prior often generated implausible artifacts. Strong gradients can push samples across object manifolds when the prior spans diverse categories. Lower gradient strengths help stabilize results, but adaptive or

class-aware gradient schedules remain an open direction.

7. Dataset

7.1. Instructions for Dataset

The dataset is constructed for low-field MRI enhancement. We first pre-train a diffusion model using axial slices from 1,000 HCP scans and simulate low-field MRI using the forward model from DynamicDPS [23]:

$$\mathcal{A}(x) = \text{Blur}(\text{DS}_k(\Gamma_\gamma(x))), \quad k = 4, \gamma = 0.7, \quad (12)$$

where Γ_γ is a gamma transform, DS_k is k -fold down-sampling, and Blur applies spatial smoothing. These parameters create a moderately ill-posed setting—severe degradation leads to uncontrolled global hallucinations, while mild degradation limits the null space needed for extrinsic cases.

We then generate 1,450 non-hallucinated predictions using DPS [10]. These serve as (i) the baseline for timestep skipping and (ii) the reference for interpolation outside the hallucination mask, ensuring hallucinations remain localized. Applying HalluGen with intrinsic and extrinsic settings produces 1,450 samples for each category, resulting in a dataset of 4,350 images in total.

The dataset consists of following: For each ground truth image x_{gt} :

- file ID and slice index for ground truth
- measurement image
- non-hallucinated baseline from DPS [10]
- intrinsic and extrinsic hallucinations from HalluGen
- binary hallucination mask for each type

All data are stored as NumPy arrays (.npy).

7.2. Computational Cost

We used $1 \times \text{A6000}$ (48GB VRAM) GPU to generate the dataset. It takes approximately 60s to generate intrinsic and 90s to generate extrinsic sample with batch size 1. However, since HVM may reject the sample with insufficient hallucination, it can take slightly longer.

7.3. Limitations

The current dataset includes only healthy adult brain MRI scans, as the diffusion prior was trained on the HCP [41]. As a result, the hallucination characteristics may not fully reflect those that occur in pathological or clinically diverse populations. Nonetheless, this release serves as an initial foundation for hallucination analysis in image restoration, providing the first controlled dataset of intrinsic and extrinsic hallucinations.

7.4. License and Ethics Statement

This work makes use of human brain MRI data provided by the Human Connectome Project (HCP) [41]. Our dataset includes ground-truth MR images obtained from HCP and synthetic hallucination outputs generated using HalluGen. All HCP images are distributed only to users who have agreed to the HCP Open Access Data Use Terms¹. Users must obtain access to the original HCP data directly from the HCP platform; we do not redistribute any HCP imaging data and do not grant additional usage rights beyond those provided by HCP.

All hallucination masks and synthetic hallucination images produced by HalluGen are released under a CC BY-NC 4.0 International License², permitting non-commercial research use with attribution. Our source code is released under the MIT License³. The dataset is intended solely for academic research and must not be used for clinical decision-making or deployed in medical settings.

No additional human subjects were recruited or scanned for this work. Our use complies with the HCP ethics and data protection policies.

8. SHAFE

8.1. Implementation Details

We provide additional implementation details for SHAFE, illustrated in Algo. 3. SHAFE is a full-reference metric that takes as input the predicted reconstruction \hat{x} and the ground-truth image x_{gt} . Both images are first passed through a low-pass filter to suppress high-frequency artifacts that do not correspond to hallucinations (e.g., checkerboard patterns), thereby reducing false positives.

Feature representations are extracted using a pre-trained encoder (e.g., DINOv3). We use multi shallow-layer features to avoid semantic bias from deeper layers and to emphasize structural and textural cues that better reflect hallucination-related deviations. Cosine distances are computed patch-wise between the feature maps of \hat{x} and x_{gt} .

Traditional image-quality metrics that aggregate patch scores uniformly (e.g., SSIM, LPIPS), but this is suboptimal for hallucination assessment, as hallucinations tend to be sparse and highly localized (see Fig. 10). To address this, inspired by soft-attention pooling [49], we apply a weighted softmax aggregation over patch-level distances, enabling SHAFE to upweight semantically abnormal regions while downweighting benign variations.

Hyperparameters. We use the following settings:

¹<https://www.humanconnectome.org/study/hcp-young-adult/document/wu-minn-hcp-consortium-open-access-data-use-terms>

²<https://creativecommons.org/licenses/by-nc/4.0/>

³<https://opensource.org/licenses/MIT>

- Low-pass filter radius: 50
- Feature backbone: DINOv3 [40], ResNet50 [51], MedSAM [9]
- Feature layer indices: [1, 2, 3], [1, 2], [-1]
- τ : 0.01, 0.01, 0.005

Algorithm 3 SHAFE: Semantic Hallucination Assessment via Feature Evaluation

Require: Prediction \hat{x} , ground truth x_{gt}

Require: Low-pass filter $\text{LP}(\cdot)$, pretrained encoder $\{f_\ell\}_{\ell \in \mathcal{L}}$ (e.g., DINOv3)

Require: Temperature $\tau > 0$

```

1:  $\tilde{x} \leftarrow \text{LP}(\hat{x}), \tilde{x}_{\text{gt}} \leftarrow \text{LP}(x_{\text{gt}})$ 
2: for each layer  $\ell \in \mathcal{L}$  do
3:    $F_\ell \leftarrow f_\ell(\tilde{x}), G_\ell \leftarrow f_\ell(\tilde{x}_{\text{gt}})$ 
4: end for
5:  $F \leftarrow \text{Concat}(\{F_\ell\}_{\ell \in \mathcal{L}}), G \leftarrow \text{Concat}(\{G_\ell\}_{\ell \in \mathcal{L}})$ 
6: Reshape  $F, G$  into patch features  $\{F_i\}_{i=1}^N, \{G_i\}_{i=1}^N$ 
7: for  $i = 1$  to  $N$  do
8:    $\delta_{\text{cos},i} \leftarrow 1 - \frac{\langle F_i, G_i \rangle}{\|F_i\|_2 \|G_i\|_2} \triangleright$  cosine distance per patch
9: end for
10:  $w_i \leftarrow \frac{\exp(\delta_{\text{cos},i}/\tau)}{\sum_{j=1}^N \exp(\delta_{\text{cos},j}/\tau)}$  for  $i = 1, \dots, N$ 
11: SHAFE  $\leftarrow \sum_{i=1}^N w_i \delta_{\text{cos},i}$ 
12: return SHAFE  $\triangleright$  optionally also return patch map  $\{w_i \delta_{\text{cos},i}\}$ 

```

8.2. Ablations

We ablate the components of SHAFE, including the low-pass (LP) filter, weighted softmax aggregation, temperature τ , and feature-layer selection. All experiments use a subset of our HalluGen dataset (N=300) for both intrinsic and extrinsic hallucinations.

Effect of Low-Pass Filtering and Weighted-softmax Aggregation. Table 6 shows that both LP filtering and weighted softmax aggregation improve hallucination detection (AUC). LP filtering suppresses high-frequency noise, helping SHAFE emphasize coherent structural differences. Weighted softmax aggregation further highlights patches with stronger feature deviations, and already outperforms uniform pooling, reflecting the spatially localized nature of hallucinations. Combining both modules increases AUC from 0.52 to 0.78, demonstrating the complementary benefits of frequency smoothing and adaptive spatial weighting.

Effect of Temperature τ . Figure 9 illustrates the impact of varying the temperature τ in the softmax aggregation. Very small values (e.g., $\tau \leq 0.001$) approximate

Table 6. Ablation of low-pass filtering (LP) and weighted-softmax aggregation in SHAFE, evaluated using AUC on hallucination detection (N=300). Both components improve detection sensitivity, and their combination yields the highest performance, indicating that suppressing high-frequency noise while adaptively weighting salient patches is crucial for detecting hallucinations.

LP	Weighted softmax	AUC
x	x	0.52
v	x	0.55
x	v	0.64
v	v	0.78

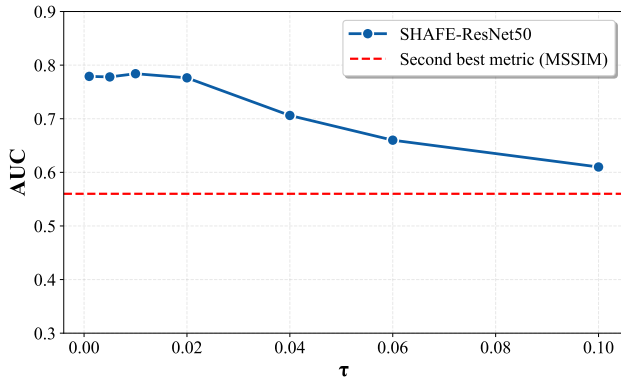


Figure 9. Effect of temperature τ in softmax aggregation for SHAFE (AUC vs. τ). Small temperatures approximate max-pooling and yield strong performance, stable until $\tau \approx 0.02$. Larger values smooth patch weighting and gradually reduce discriminability, yet SHAFE remains superior to the second-best metric across all tested values.

max-pooling and already produce strong AUC, indicating that hallucinations often manifest as localized feature deviations. Performance remains stable until $\tau \approx 0.02$, after which AUC decreases gradually as the softmax distribution becomes more uniform and less discriminative. Nonetheless, SHAFE continues to outperform the second-best baseline across all tested values, highlighting robustness to τ .

Impact of Feature-Layer Selection. Table 7 reports the effect of feature-layer selection when using SHAFE-ResNet50. Using only deeper layers degrades performance, likely due to dataset-specific and task-specific bias that do not fully align with medical and industrial domains. Shallow features capture texture and low-level structure, which are more sensitive to fine-grained hallucinations. The best performance is achieved when combining multiple shallow layers (AUC=0.78), supporting our design choice that multi-layer early features provide richer representations for hallucination scoring.

Table 7. Impact of feature-layer selection on SHAFE hallucination detection (AUC, N=300) using SHAFE-ResNet50. Deep layers alone degrade performance due to semantic bias from ImageNet pretraining, whereas combining shallow layers provides the highest AUC, supporting the use of multi-layer early features for hallucination sensitivity.

Layer 1	Layer 2	Layer 3	AUC
v	x	x	0.75
x	v	x	0.76
x	x	v	0.63
v	v	x	0.78
v	v	v	0.72

8.3. Localization

Fig. 10 presents the localization performance of SHAFE on both HalluGen samples and real restoration outputs generated by ESRGAN [44] and SwinIR [30]. SHAFE consistently highlights hallucinated regions such as distorted lateral ventricles and disrupted sulcal boundaries, demonstrating its ability to detect both synthetic and naturally occurring failures. The resulting heatmaps are characteristically sparse, emphasizing localized deviations rather than diffuse artifacts. This sparsity further justifies the use of weighted softmax aggregation over uniform pooling, as it enables SHAFE to selectively amplify subtle but semantically meaningful hallucinated features.

8.4. Limitations of SHAFE

Fig. 11 illustrates representative limitations of SHAFE. First, SHAFE is less sensitive to high-frequency artifacts (e.g., periodic grid patterns) due to the low-pass filtering step, which suppresses high-frequency content because hallucinations in our taxonomy mainly occur in the low- to mid-frequency range. Consequently, images with such artifacts may obtain SHAFE scores similar to clean ones. Second, SHAFE can assign high responses to large intensity differences in semantically uninformative regions, such as brain boundaries, where intensity mismatches are high but structural deviation is minimal.

8.5. Inference Speed

Fig. 12 compares the inference time of SHAFE-ResNet50 with baseline metrics in our hallucination benchmark. While SHAFE is naturally slower than pixel-based metrics such as PSNR and SSIM, it remains significantly more efficient than feature-based alternatives: SHAFE is about $2.4\times$ faster than LPIPS and $9\times$ faster than DISTS. This shows that the combination of low-pass filtering, shallow feature extraction, and weighted softmax aggregation provides strong detection performance without the heavy computational cost of deep feature metrics. All timings were measured on a local machine with an AMD Ryzen 7 CPU.

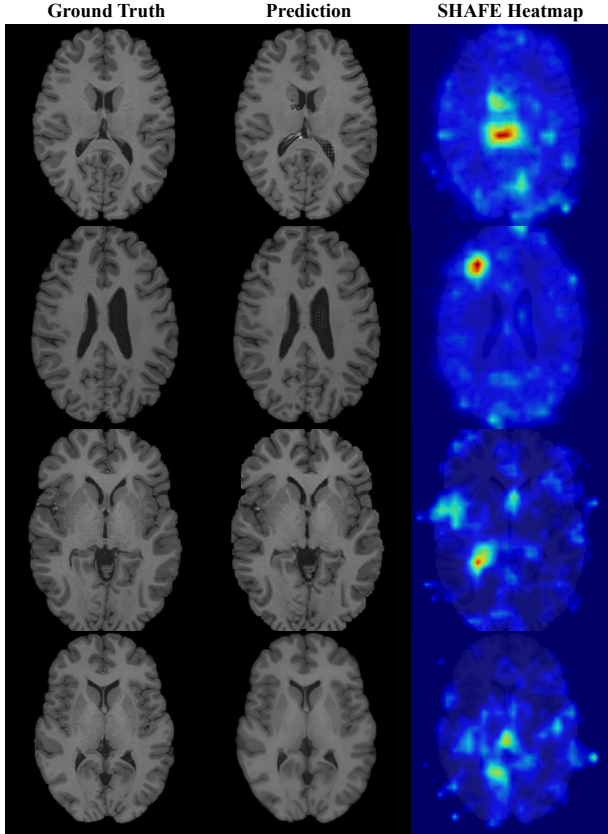


Figure 10. **Visual results of SHAFE heatmap on both synthetic (HalluGen) and real restoration outputs.** First and second rows are extrinsic and intrinsic examples from HalluGen and third and fourth are real restoration outputs from ESRGAN and SwinIR.

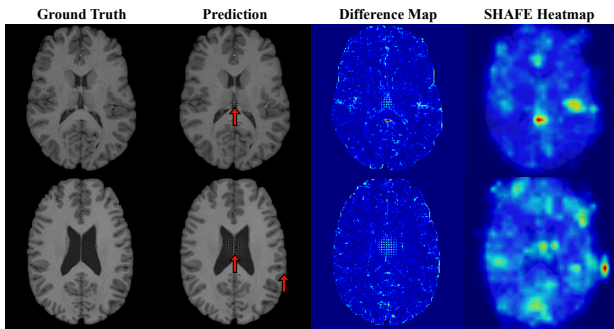


Figure 11. **Visual examples of SHAFE limitations (red arrows).** SHAFE is less sensitive to high-frequency reconstruction artifacts (e.g., periodic grid patterns) due to the use of low-pass filtering, which suppresses non-semantic noise. In addition, SHAFE may highlight boundary regions where intensity differences are large but carry limited semantic relevance.

9. Reference-free Hallucination Detector

We describe the architecture of our reference-free hallucination detector. As shown in Fig. 13, the detector takes the

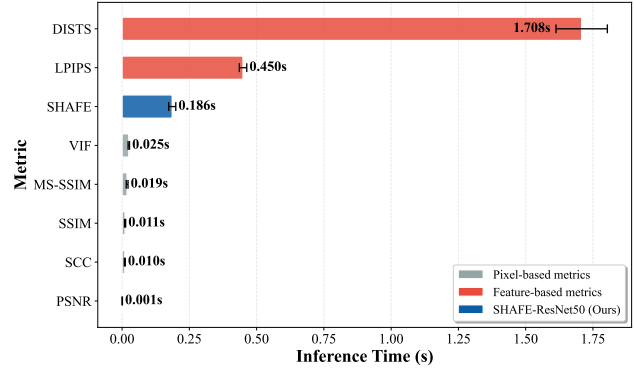


Figure 12. **Inference time comparison for baseline metrics vs. SHAFE-ResNet50.** Despite using feature extraction and weighted softmax, SHAFE remains computationally efficient, running significantly faster than other feature-based metrics such as LPIPS and DISTs. This demonstrates that SHAFE achieves superior detection performance without incurring substantial computational overhead. AMD Ryzen 7 CPU was used for testing.

measurement y and predicted reconstruction \hat{x} as inputs, both of which are first low-pass filtered to suppress high-frequency noise. The filtered images are passed through a shallow ResNet-50 feature extractor, and their features are concatenated before a binary classification head. We also experimented with concatenating the raw inputs prior to feature extraction, but this caused the model to focus on low-level differences (e.g., small shifts or texture changes) rather than true semantic discrepancies. The detector is trained with cross-entropy loss for 100 epochs using a learning rate of 0.001 on HalluGen-generated samples. Because it relies only on the measurement–prediction pair, the detector supports fully reference-free hallucination detection.

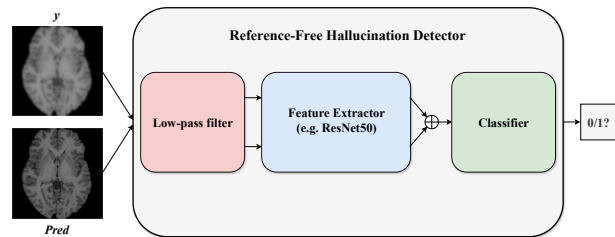


Figure 13. **Network architecture of reference-free hallucination detector.** Prediction and measurement images are fed into the model, applied low-pass filter to remove high-frequency noise and then classified using a simple CNN architecture such as ResNet50.

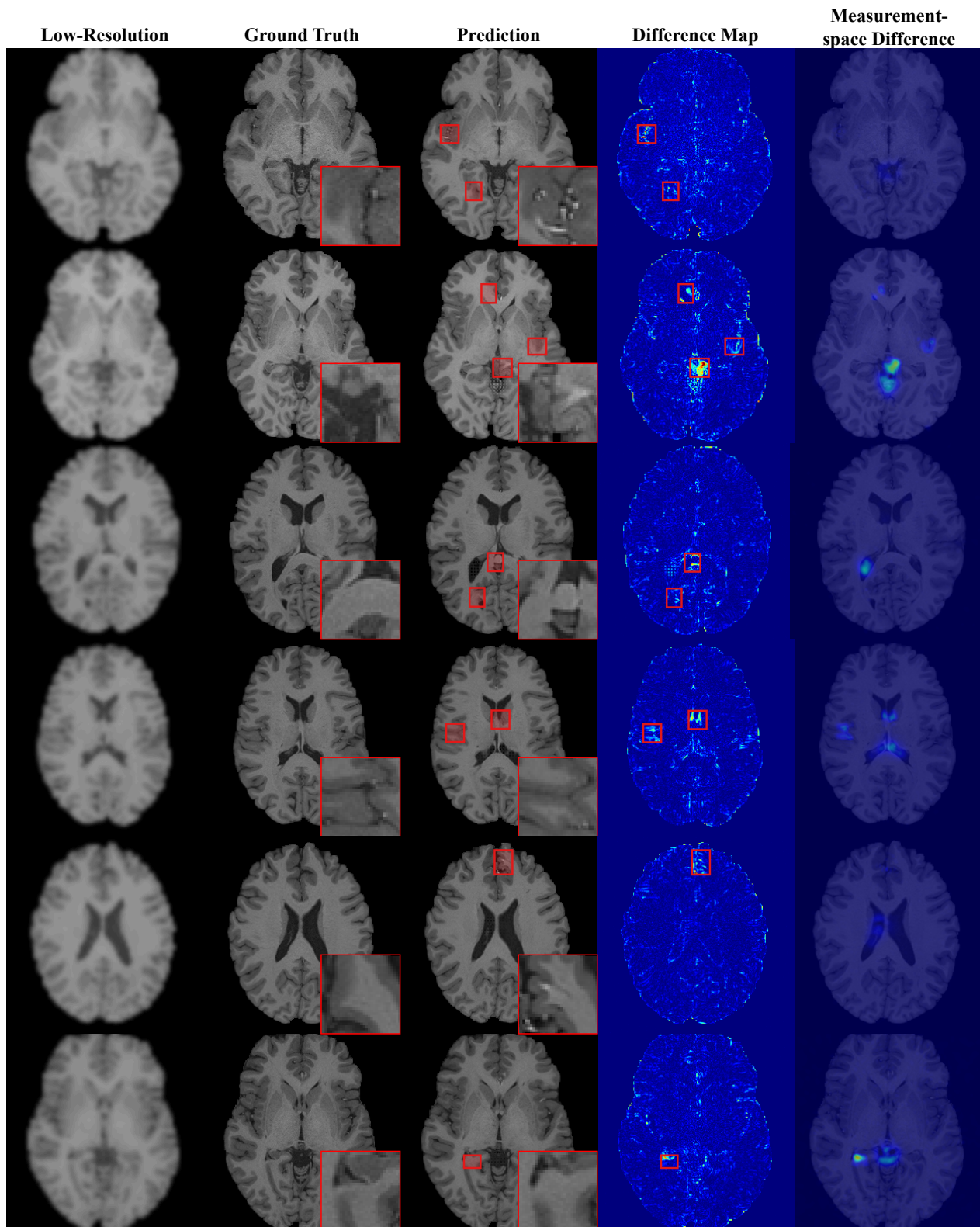


Figure 14. **Visual results of HalluGen examples on brain MRI.** Odd-numbered rows show intrinsic hallucinations, and even-numbered rows show extrinsic hallucinations.

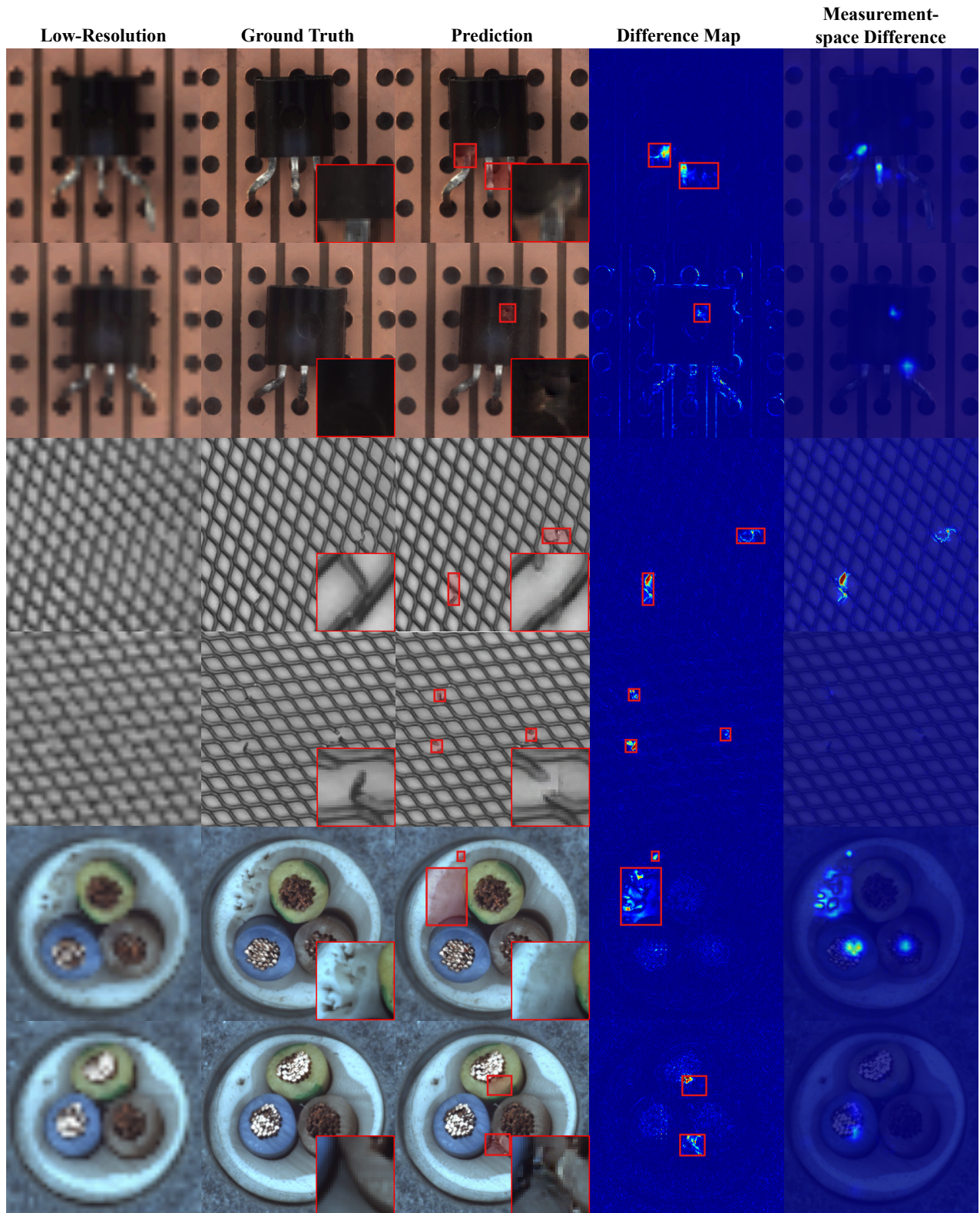


Figure 15. **Visual results of HalluGen examples on MVTec AD.** Odd-numbered rows show extrinsic hallucinations, and even-numbered rows show intrinsic hallucinations. Row 4 and 5 use ground truth mask from MVTec AD to show the flexibility of HalluGen with different size and shape of masks.

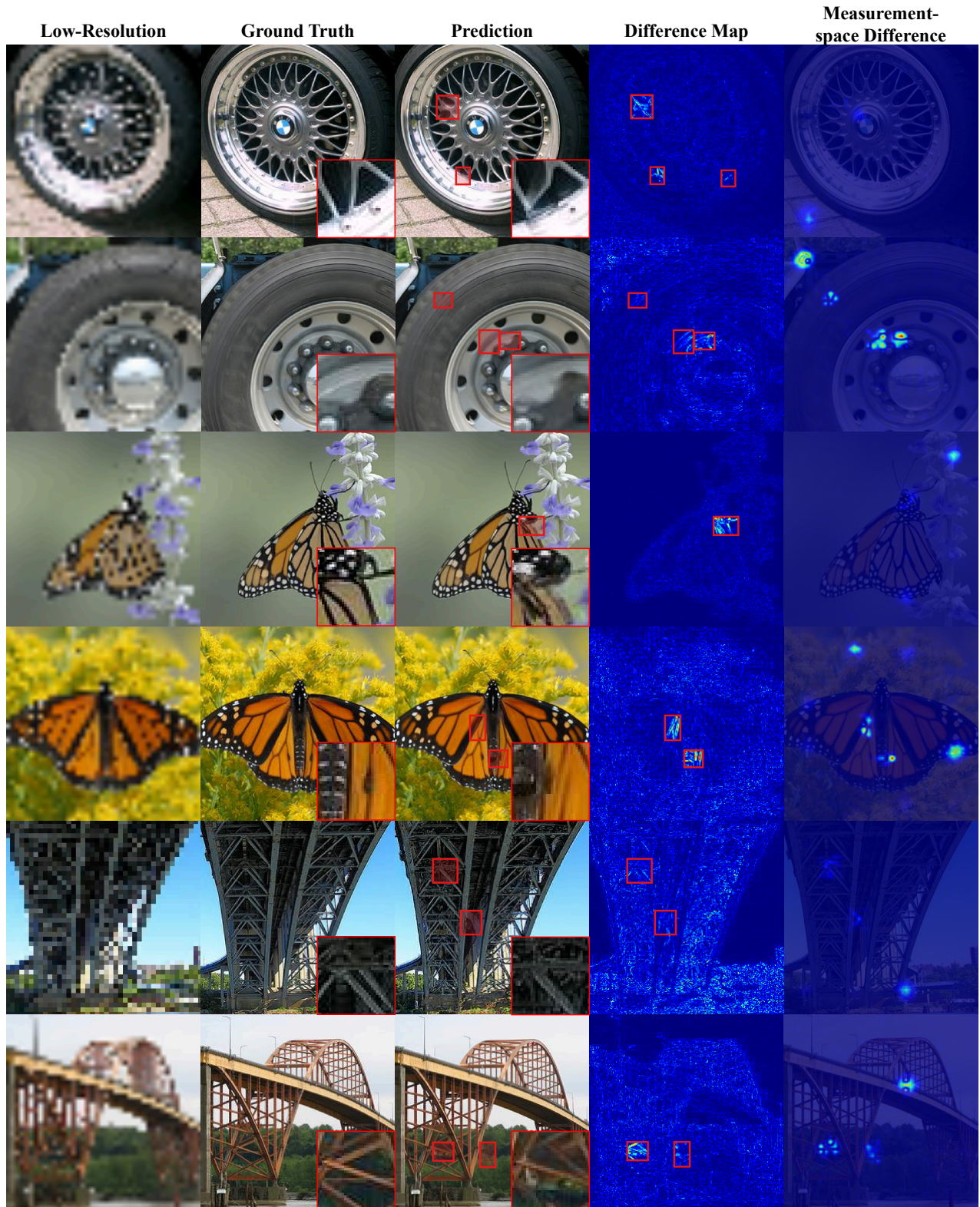


Figure 16. Visual results of HalluGen examples on ImageNet. Odd-numbered rows show extrinsic hallucinations, and even-numbered rows show intrinsic hallucinations.